The Astronomical Journal, 168:91 (12pp), 2024 August https://doi.org/10.3847/1538-3881/ad53bf

TOI-1173 A *b*: The First Inflated Super-Neptune in a Wide Binary System

Jhon Yana Galarza[1,9], Thiago Ferreira[2], Diego Lorenzo-Oliveira[3], Joshua D. Simon[1], Henrique Reggiani[4], Anthony L. Piro[1], R. Paul Butler[5], Yuri Netto[6], Adriana Valio[6], David R. Ciardi[7], and Boris Safonov[8]
[1] The Observatories of the Carnegie Institution for Science, 813 Santa Barbara Street, Pasadena, CA 91101, USA; jyanagalarza@carnegiescience.edu
[2] Department of Astronomy, Yale University, 219 Prospect Street, New Haven, CT 06511, USA
[3] Laboratório Nacional de Astrofísica, Rua Estados Unidos 154, 37504-364, Itajubá—MG, Brazil
[4] Gemini South, Gemini Observatory, NSF's NOIRLab, Casilla 603, La Serena, Chile
[5] Earth and Planets Laboratory, Carnegie Institution for Science, 5241 Broad Branch Road, NW, Washington, DC 20015, USA
[6] Center for Radio Astronomy and Astrophysics Mackenzie (CRAAM), Mackenzie Presbyterian University, Rua da Consolação, 896, São Paulo, Brazil
[7] NASA Exoplanet Science Institute, IPAC, California Institute of Technology, Pasadena, CA 91125, USA
[8] Sternberg Astronomical Institute Lomonosov Moscow State University, Russia
Received 2024 March 9; revised 2024 May 14; accepted 2024 June 2; published 2024 July 25

Abstract

Among Neptunian mass exoplanets ($20-50\,M_{\oplus}$), puffy hot Neptunes are extremely rare, and their unique combination of low mass and extended radii implies very low density ($\rho < 0.3$ g cm^{-3}). Over the last decade, only a few puffy planets have been detected and precisely characterized with both transit and radial velocity observations, most notably including WASP-107 *b*, TOI-1420 *b*, and WASP-193 *b*. In this paper, we report the discovery of TOI-1173 A *b*, a low-density ($\rho = 0.195^{+0.018}_{-0.017}$ g cm^{-3}) super-Neptune with $P = 7.06$ days in a nearly circular orbit around the primary G-dwarf star in the wide binary system TOI-1173 A/B. Using radial velocity observations with the MAROON-X and HIRES spectrographs and transit photometry from TESS, we determine a planet mass of $M_{\rm p} = 27.4 \pm 1.7\,M_{\oplus}$ and radius of $R_{\rm p} = 9.19 \pm 0.18\,R_{\oplus}$. TOI-1173 A *b* is the first puffy super-Neptune planet detected in a wide binary system (projected separation ∼11,400 au). We explore several mechanisms to understand the puffy nature of TOI-1173 A *b* and show that tidal heating is the most promising explanation. Furthermore, we demonstrate that TOI-1173 A *b* likely has maintained its orbital stability over time and may have undergone von-Zeipel–Lidov–Kozai migration followed by tidal circularization, given its present-day architecture, with important implications for planet migration theory and induced engulfment into the host star. Further investigation of the atmosphere of TOI-1173 A *b* will shed light on the origin of close-in low-density Neptunian planets in field and binary systems, while spin–orbit analyses may elucidate the dynamical evolution of the system.

Unified Astronomy Thesaurus concepts: Exoplanets (498); Hot Neptunes (754); Wide binary stars (1801); Radial velocity (1332); Transit photometry (1709); Exoplanet detection methods (489); Exoplanet astronomy (486); Transits (1711)

1. Introduction

The discovery of 51 Peg *b* (Mayor & Queloz 1995) revolutionized our understanding of planet formation and evolution due to the surprising result that gas-giant planets could be observed relatively close to main-sequence stars. This finding hints not only that exoplanets are formed through core accretion of gaseous protoplanetary disk material (Pollack et al. 1996), but also that it is possible that planets might originate at a wide distance from their host star and subsequently undergo migration (Rice & Armitage 2003; Ida & Lin 2004). In a similar aspect, despite exhibiting similar masses to the solar system gas-/ice-giant planets, inflated radii planets present an enigma, boasting extended and diffuse atmospheres that defy conventional models for planet formation and evolution (e.g., Lopez & Fortney 2014; Lee & Chiang 2015 and references therein). These planets constitute a category characterized by an uncommon combination of large sizes and exceptionally low densities ($\rho \leqslant 0.3$ g cm^{-3}), aptly named puffy[10] planets.

Their proximity to their host stars could be responsible for the heating and expansion of their atmospheres (Batygin & Stevenson 2010; Pu & Valencia 2017; Thorngren & Fortney 2018), which contributes to their observed low density. For objects with equilibrium temperatures exceeding 1000 K, the inflated radius mechanism may be similar to hot Jupiter planets (Fortney et al. 2021), i.e., (a) due to the thermal contraction of He/H atmospheres (Owen & Wu 2013; Lopez & Fortney 2014), (b) atmospheric winds driven by photoionization due to intense UV radiation from the host star (Murray-Clay et al. 2009), which can be probed by observing the larger transit depths due to atmospheric expansion in the Lyα line at $\lambda = 1215.6$ Å signatures in a planet's spectrum (Kislyakova et al. 2019; Owen et al. 2023), Hα absorption at $\lambda = 6562.8$ Å (Jensen et al. 2012; Christie et al. 2013; Cauley et al. 2017), or the Helium triplet in the near-infrared at $\lambda = 10833$ Å (Spake et al. 2018; dos Santos et al. 2020; Vissapragada et al. 2020; Orell-Miquel et al. 2022; Bennett et al. 2023; Krolikowski et al. 2024), and/or (c) photochemical hazes in the atmosphere responsible for a larger and puffier appearance (Gao & Zhang 2020;

[9] Carnegie Fellow.

[10] Super-puff planets are worlds with core masses ($\leqslant 5M_{\oplus}$) but with radii comparable to gas giants ($\geqslant 4R_{\oplus}$), leading to extremely low densities ($\leqslant 0.1$ g cm^{-3}).

Ohno & Tanaka 2021). Nevertheless, these mechanisms may not fully elucidate the large radii observed in the lowest-density planets with equilibrium temperatures below 1000 K, which poses an additional challenge in incorporating such phenomena into existing exoplanet formation models.

Puffy planets are extremely rare, with only five planets in the intermediate-mass regime ($20M_{\oplus} \leqslant M_p \leqslant 50M_{\oplus}$) with densities below $\rho \leqslant 0.3$ g cm^{-3} (per The Extrasolar Planets Encyclopædia[11] as of 2024 March) in single stars and none detected in binary systems. These exoplanets are HATS-8 *b* (Bayliss et al. 2015), TOI-1420 *b* (Yoshida et al. 2023), TOI-2525 *b* (Trifonov et al. 2023), WASP-107 *b* (Anderson et al. 2017), and WASP-193 *b* (Barkaoui et al. 2024), which were detected by both the radial velocity and transit methods. Planets in this category are intrinsically important in deciphering the mechanisms that lead to runaway gaseous accretion, despite their smaller cores, a phenomenon crucial to our understanding of planetary formation and evolution (Lissauer & Stewart 1993; Bitsch et al. 2015). It is noteworthy that only two objects in this sample (TOI-2525 *b* and WASP-107 *b*) belong to multiplanet systems and all orbit stars with effective temperatures above 4400 K.

This paper presents the discovery of a low-density inflated super-Neptune ($M_{\rm p} = 27.4\,M_{\oplus}$) found in orbit around an 8.7 Gyr old G-dwarf star, completing each orbit in ∼7.064 days. The TOI-1173 system contains two stars, the planet-hosting component, TOI-1173 A, and TOI-1173 B, which lacks any detected exoplanets (J. Yana Galarza et al. 2024, in preparation). This system is the second wide binary with a separation greater than 10,000 au discovered to host planets after HAT-P-4 A (29,500 au; Mugrauer et al. 2014).

In Section 2, we describe the spectroscopic and photometric observations of TOI-1173 A with the M dwarf Advanced Radial velocity Observer Of Neighboring eXoplanets (MAROON-X) and TESS, respectively. In Section 3, we present a Keplerian model, and in Section 4, we discuss the origin of the close-in low-density nature of TOI-1173 A *b* plus the relevant timescales for the dynamical evolution of this TOI-1173 A/B system. Last, we provide an overview of our findings and discuss future research prospects in Section 5.

2. Observations

2.1. Transiting Exoplanet Survey Satellite Photometry

TOI-1173 A (TIC 232967440) was observed by the Transiting Exoplanet Survey Satellite (TESS; Ricker et al. 2015) during Sectors 14, 15, 21, 22, 41, 47, 48, 74, and 75. The TESS light curves of TOI-1173 A[12] revealed several periodic transits, leading to the detection and announcement of TOI-1173 A *b* (TOI-1173.01)[13] as a transiting planet candidate by the TESS Science Office (Guerrero et al. 2021). TOI-1173 A is a component of a binary system, and their projected separation is ∼86″ (El-Badry et al. 2021). We used TPFPLOTTER[14] (Aller et al. 2020) to check for contamination by the companion star (TOI-1173 B) in the automatically selected aperture. The target pixel file for the pair is displayed in Figure 1, showing that the components are not blended in TESS. We retrieved the 2 minute cadence observations, which were processed by the

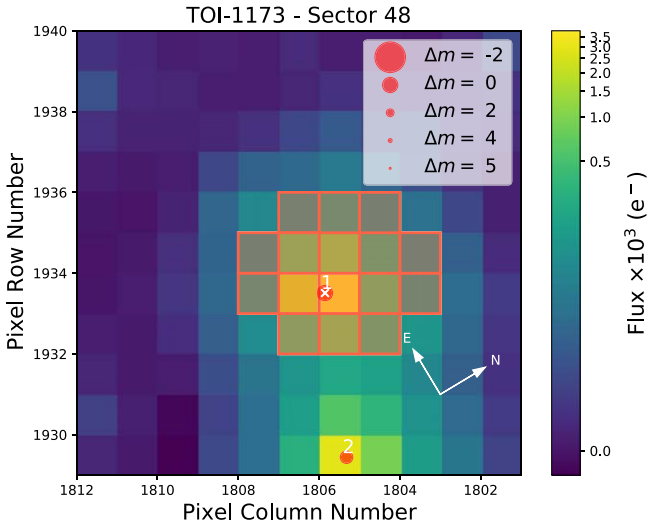

Figure 1. Target pixel file of TOI-1173 A (white cross) from the TESS observations in Sector 48. The SPOC pipeline aperture is overplotted with shaded red squares, clearly showing that there is no contamination by the companion star TOI-1173 B (marked with the number 2). The projected separation between the components (numbers 1 and 2) is ∼86″.

Science Processing Operations Center (SPOC; Jenkins et al. 2016) standard aperture pipeline, which provides systematics-corrected Presearch Data Conditioning (PDC) photometry (Smith et al. 2012; Stumpe et al. 2012), using the LIGHTKURVE[15] software (Lightkurve Collaboration et al. 2018).

To remove systematic instrumental trends characterized by a gradual increase/decrease in the apparent stellar flux over time, we applied a detrending model to the PDC light curve, using the wōTAN[16] package (Hippke et al. 2019) with a window length of 0.4 and using the Cosine Filtering with Autocorrelation Minimization (Kipping et al. 2013) algorithm. To minimize the impact of the trend removal filter on the transit shape, we mask the transits using the TRANSIT_MASK feature in wōTAN. The PDC-detrended light curves of all sectors are depicted in the lower panels of Figure 2, and we retrieved a prominent modulation period of 7.066 days using a Box-fitting Least Squares (BLS) algorithm[17] (Kovács et al. 2002; Bhatti & Bouma 2021) in a period grid spanning from 0.25 to 100 days (see the upper panel of Figure 2).

2.2. MAROON-X and High Resolution Echelle Spectrometer Radial Velocities

To confirm the planetary nature of the transit signal, we obtained 10 epochs of spectroscopy of TOI-1173 A with the high-resolution echelle spectrograph MAROON-X (Seifahrt et al. 2018, 2022), mounted on the 8.1 m Gemini North Telescope of The International Gemini Observatory located in Hawaii (program ID GN-2022A-Q-227; PI: Yuri Netto). The MAROON-X data were reduced using a custom Python 3 data reduction, which is incorporated into Gemini's DRAGON platform. The planet-hosting TOI-1173 A was also observed with the High Resolution Echelle Spectrometer (HIRES; Vogt et al. 1994) at the Keck observatory. The public HIRES spectra were downloaded through the Keck Observatory Archive[18] using the Program IDs: C258_2020A

[11] https://exoplanet.eu/home/
[12] All the TESS data used in this paper can be found in MAST at doi:10.17909/dpx3-gv19.
[13] https://exo.mast.stsci.edu/exomast_planet.html?planet=TOI1173.01
[14] https://github.com/jlillo/tpfplotter
[15] https://docs.lightkurve.org/
[16] https://github.com/hippke/wotan
[17] https://astrobase.readthedocs.io/
[18] https://koa.ipac.caltech.edu/cgi-bin/KOA/nph-KOAlogin

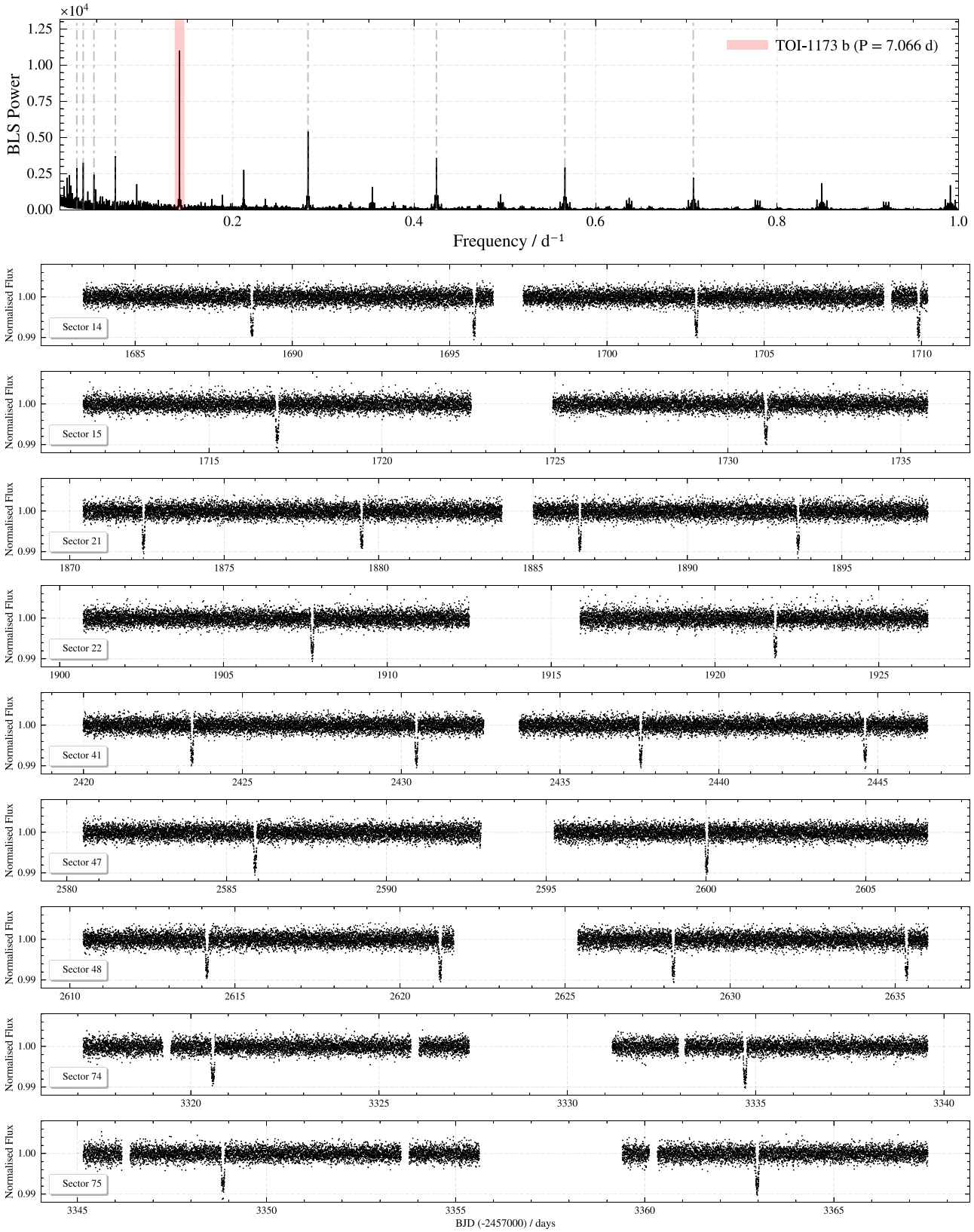

Figure 2. Upper panel: BLS periodogram for TOI-1173 A *b*'s observations. The prominent period of $P = 7.066$ days is indicated as a red strip, along with lower (P/n, $n = 1, 2, 3, 4$) and upper ($P \times n$) harmonics, in gray. Bottom panels: detrended TESS 2 minute cadence PDC light curves. Transit events are visible every 7.066 days.

(PI: Dai), H070_2020B (PI: Weiss), N062_2020B (PI: Weiss), C247_2020B (PI: Dai), U006_2020B (PI: Robertson), N180_2021A (PI: Crossfield), N012_2021A (PI: Howard), U111_2021A (PI: Batalha), H280_2021B (PI: Brinkman), U114_2021B (PI: Dressing), C260_2021B (PI: Dai), Y166_2022A (PI: Louden), U072_2022A (PI: Kane),

Table 1
Radial Velocities for TOI-1173 A Collected with the MAROON-X/Gemini and HIRES/Keck Spectrographs

MAROON-X			
Time (BJD)	ΔRV (m s^{-1})	σ_{RV} (m s^{-1})	Channel
2459677.98023	−6.24	1.57	Blue
2459678.95631	−11.74	1.54	Blue
2459680.86707	−6.32	1.57	Blue
2459682.93170	8.07	1.18	Blue
2459688.97070	1.05	1.41	Blue
2459690.00549	5.50	1.02	Blue
2459696.89675	6.52	1.03	Blue
2459780.77974	0.62	1.00	Blue
2459791.74470	−10.06	1.67	Blue
2459792.74451	−12.01	1.27	Blue
2459677.98023	−10.02	2.66	Red
2459678.95631	−13.25	2.60	Red
2459680.86707	−3.23	2.64	Red
2459682.93170	7.36	2.04	Red
2459688.97070	1.35	2.39	Red
2459690.00549	4.75	1.80	Red
2459696.89675	4.09	1.80	Red
2459780.77974	3.97	1.83	Red
2459791.74470	−5.79	3.00	Red
2459792.74451	−9.46	2.25	Red
HIRES			
Time (BJD)	ΔRV (m s^{-1})	σ_{RV} (m s^{-1})	
2458885.00826	10.14	1.70	
2459077.78600	0.00	1.80	
2459101.73272	−4.98	1.82	
2459190.16130	−2.09	1.86	
2459215.11314	−2.59	1.88	
2459271.95793	−0.59	1.95	
2459353.81030	11.43	1.59	
2459378.85255	10.72	1.72	
2459435.76640	10.10	1.80	
2459470.73257	11.16	1.67	
2459566.15808	12.26	1.95	
2459593.15571	4.02	1.73	
2459632.97939	9.78	1.75	
2459662.02642	4.99	2.23	
2459690.97466	2.52	1.92	
2459715.96062	−7.21	1.77	
2459739.82355	4.05	1.76	
2459771.83594	16.02	1.85	
2459792.76457	10.21	1.90	
2459826.74058	−8.22	1.71	

H258_2022A (PI: Bottom), C279_2022A (PI: Zink), and C342_2022B (PI: Howard). In total, we retrieved 20 spectra with a spectral resolution of $R = \lambda/\Delta\lambda = 48{,}000$ and signal-to-noise ratios (SNRs) ranging from 100 to 150 on the red chip. The radial velocities were calculated using the iodine cell technique, as described in detail in Butler et al. (1996, 2017). Both the MAROON-X and HIRES radial velocities are listed in Table 1.

We employed the Generalized Lomb–Scargle method (Zechmeister & Kürster 2009) on a grid ranging from 0.1 to 200 days and detected a highly significant periodic signal at $P_{LS} = 7.076$ days, which is in line with the period found in the TESS data, with a relative difference of $\Delta P = 0.009$ days. A Bayesian Information Criterion (BIC) test (Ivezić et al. 2014) revealed a discrepancy of $\Delta\mathrm{BIC} \approx 400$ between a periodic model and a nonvarying model.

Stellar activity may sometimes simply add noise to the data, but in the worst scenario, it can mimic or masquerade as planetary signals. Therefore, we analyzed five stellar activity proxies for TOI-1173 A using the SpEctrum Radial Velocity AnaLyser SERVAL pipeline[19] (Zechmeister et al. 2018): the differential line width (dLW), chromatic index (CrX), Hα ($\lambda = 656.46$ nm), and Na D doublet ($\lambda = 589.0$ nm and 589.6 nm) for the Blue channel, as well as the Ca II IRT1, IRT2, and IRT3 infrared triplet ($\lambda = 849.8$, 854.2, and 866.2 nm) for the Red channel of the MAROON-X spectra.

At the companion's orbital period, we did not observe any indication of significant timing or phase modulations, which could commonly arise if the period were due to stellar activity cycles, such as atmospheric expansions or pulsations (e.g., Sobolev 1960; Doazan & Peton 1970). Furthermore, we did not detect statistically meaningful correlations between these magnetic activity indicators and the radial velocity measurements, as evaluated by the Pearson r correlation index and the null-hypothesis significance-testing p-value (see Figure 3). This analysis strengthens the evidence in favor of a companion nature for the observed radial velocity variations at the retrieved prominent modulation period, and even in the presence of any significant stellar magnetic activity, we do not expect suppression of the companion's signal.

2.3. Stellar Parameters of the Binary System

TOI-1173 A is the primary component of the binary system TOI-1173 A/B. This pair was first reported as a wide binary system by El-Badry et al. (2021). The two stars are separated by approximately ∼86″ in the sky, and only the A component harbors an exoplanet. We obtained MAROON-X spectra for both components with high spectral resolution ($R = 85{,}000$) and SNR (∼300). We determined the stellar parameters of the pair—meaning the effective temperature, surface gravity, metallicity, and microturbulence velocity—using the differential approach. We estimated the mass, radius, and age using the isochrone-fitting method. The methodology is thoroughly explained in our companion paper (J. Yana Galarza et al. 2024, in preparation). The results are listed in Table 2. Both components are old and slightly metal-rich stars, with TOI-1173 A being a G9-type star and TOI-1173 B a K1.5-type star.

2.4. High-resolution Imaging

As part of our standard process for validating transiting exoplanets to assess the possible contamination of bound or unbound companions on the derived planetary radii (Ciardi et al. 2015), we observed TOI-1173 A with high-resolution near-infrared adaptive optics (AO) imaging at the Keck Observatory.

2.4.1. Near-infrared AO at Keck

The observations were made with the NIRC2 instrument on Keck II behind the natural guide-star AO system (Wizinowich et al. 2000) on 2020 May 28 UT in the standard three-point dither pattern that is used with NIRC2 to avoid the left lower quadrant of the detector, which is typically noisier than the

[19] https://github.com/mzechmeister/serval

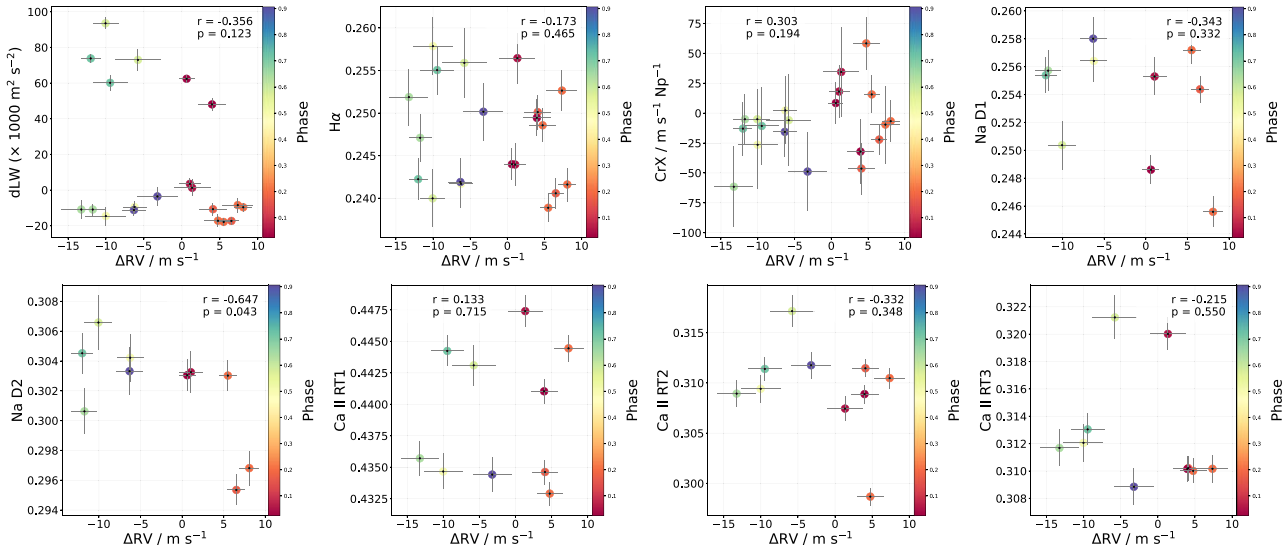

Figure 3. Radial velocity and the relationship with TOI-1173 A's activity indicators dLW, CrX, and Hα, plus the Na doublet for the Blue channel and the Ca II infrared triplet for the Red channel of MAROON-X spectra. The colors indicate the phase at $P_{\rm LS} = 7.076$ days. The Pearson r correlation index and the associated p-values are indicated at the top of each panel.

Table 2
Fundamental Parameters of the Wide Binary System TOI-1173 A/B

Parameter	TOI-1173 A	TOI-1173 B
Effective temperature (K)	5350 ± 34	5047 ± 34
Surface gravity (dex)	4.450 ± 0.020	4.53 ± 0.030
Metallicity (dex)	0.139 ± 0.065	0.114 ± 0.069
Microturbulence (km s^{-1})	1.11 ± 0.01	1.09 ± 0.01
Age (Γ, Gyr)	$8.7^{+2.0}_{-1.9}$	$8.6^{+3.1}_{-3.5}$
Mass ($M_\odot$)	$0.911^{+0.028}_{-0.030}$	$0.839^{+0.033}_{-0.036}$
Radius ($R_\odot$)	$0.934^{+0.011}_{-0.011}$	$0.820^{+0.010}_{-0.011}$
$v \sin i$ (km s^{-1})	<2.0	<2.0

other three quadrants. The dither pattern step size was 3″ and was repeated twice, with each dither offset from the previous dither by 0.″5. NIRC2 was used in the narrow-angle mode with a full field of view of ∼10″ and a pixel scale of approximately 0.″0099442 per pixel. The Keck observations were made in the Br–γ filter ($\lambda_o = 2.1686$; $\Delta\lambda = 0.0326\,\mu$m) with an integration time in each filter of 3 s, for a total of 27 s.

Flat fields were generated from a median average of dark-subtracted dome flats. Sky frames were generated from the median average of the nine dithered science frames; each science image was then sky-subtracted and flat-fielded. The reduced science frames were combined into a single image using an intrapixel interpolation that conserves flux and shifts the individual dithered frames by the appropriate fractional pixels; the final resolution of the combined dithers was determined from the FWHM of the point-spread function: 0.″0494. To within the limits of the AO observations, no stellar companions were detected. The final 5σ limit at each separation was determined from the average of all the determined limits at that separation and the uncertainty on the limit was set by the rms dispersion of the azimuthal slices at a given radial distance (see the left panel of Figure 4).

2.4.2. Optical Speckle

We observed TOI-1173 on 2020 November 29 UT with the Speckle Polarimeter (Safonov et al. 2017) on the 2.5 m telescope at the Caucasian Observatory of the Sternberg Astronomical Institute (SAI) of Lomonosov Moscow State University. The Electron Multiplying CCD Andor iXon 897 was used as a detector. The atmospheric dispersion compensator allowed observation through the wideband I_c filter. The power spectrum was estimated from 4000 frames with 30 ms exposure times. The detector has a pixel scale of 20.6 mas pixel^{-1}, and the angular resolution was 89 mas. The long-exposure seeing was 1.″07. We did not detect any stellar companions brighter than $\Delta I_C = 4.3$ and 6.5 at $\rho = 0.''25$ and 1.″0, respectively, where ρ is the separation between the source and the potential companion. The speckle image is depicted in the right panel of Figure 4.

Furthermore, we also found independent analyses in the ExoFOP database based on ground-based time series of TOI-1173 A. These results confirm that the transit is caused by an exoplanet, a conclusion supported by our estimated transit and radial velocity periods.

3. Keplerian Fit

We employed the ALLESFITTER[20] software (Günther & Daylan 2021) for a joint transit and radial velocity Keplerian fit of TOI-1173 A b, with free parameters including the orbital period (P), time of inferior conjunction (T_0), Doppler-induced radial velocity semi-amplitude (K), cosine of the orbital inclination ($\cos i$), sum of stellar and companion radii divided by the semimajor axis ($(R_p + R_\star)/a$), limb-darkening coefficients q_1 and q_2 (see Kipping 2013 and Espinoza & Jordán 2016 for details), plus jitter terms for TESS and both MAROON-X channels. Considering also the possibility of another orbiting companion to TOI-1173 A, or that the modulations were in part due to stellar activity, we set uniform priors for the model barycenter motion $\dot{\gamma}$ and radial velocity intercept γ. These parameters are incorporated into the model in the form $\gamma + \dot{\gamma} \cdot (T - T_0)$, where T represents the time of the observations. Furthermore, we set the orbital eccentricity plus periastron argument coupled as Laplace parameters $\sqrt{e}\cos(\omega)$ and

[20] https://www.allesfitter.com/

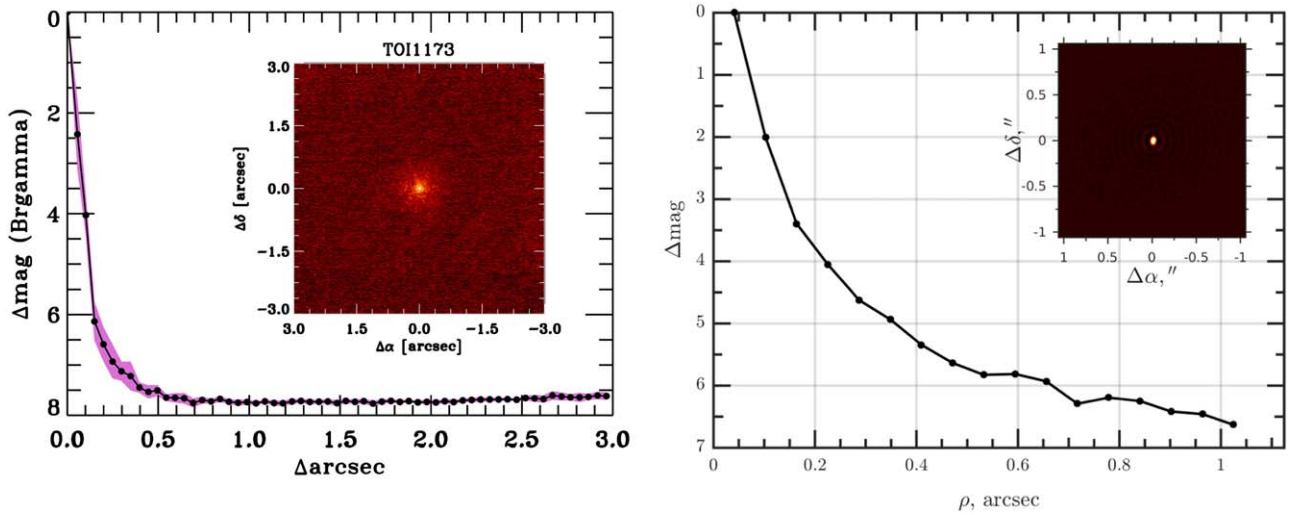

Figure 4. Left: companion sensitivity for the near-infrared AO imaging. The black points represent the 5σ limits and are separated in steps of 1 FWHM. The purple represents the azimuthal dispersion (1σ) of the contrast determinations (see the text). The inset image is of the primary target showing no additional close-in companions. Right: SAI 2.5 m I_c-band speckle sensitivity curve for TOI-173 A. The speckle image also does not show evidence of close companions.

$\sqrt{e}\sin(\omega)$ to avoid Lucy–Sweeney degeneracy (Lucy & Sweeney 1971).

The Markov hyperparameter space in this Keplerian model was also probed using DYNESTY over 500 live points and tolerance of the convergence criterion of 0.01 (see the details in Günther & Daylan 2021). The resulting parameters indicate a planet with mass $27.4 \pm 1.7\ M_{\oplus}$, radius $9.19 \pm 0.18\ R_{\oplus}$, and density $0.195^{+0.018}_{-0.017}$ g cm^{-3} in a nearly circular ($e = 0.023$) orbit around TOI-1173 A every 7.06466 days (see Table 3 for the full Keplerian parameters). Figure 5 presents the best-fit one-companion joint model for TOI-1173 A *b*.

4. Discussion

4.1. TOI-1173 A b: A Low-density Super-Neptune

In Figure 6, we present the discovery of TOI-1173 A *b* in context, on a mass–radius (M–R) diagram of other super-Neptune planets ($20M_{\oplus} \leqslant M_p \leqslant 50M_{\oplus}$) from the Encyclopædia of Exoplanetary Systems as of 2024 March. The near neighbors to TOI-1173 A *b* are TOI-2525 *b* (Trifonov et al. 2023), WASP-107 *b* (Piaulet et al. 2021), and TOI-1420 *b* (Yoshida et al. 2023). The latter two are important targets for studies of planetary atmospheres. Both exoplanets share similar periods, masses, eccentricities, and semimajor axes as TOI-1173 A *b*, but have larger radii, which leaves TOI-1173 A *b* somewhat denser than WASP-107 *b* and TOI-1420 *b*. Nonetheless, this comparison is relative to single stars. TOI-2525 *b* is an inflated exoplanet orbiting a K-dwarf star. However, it differs from TOI-1173 A *b* in its longer period (23 days), higher eccentricity (0.17), and larger semimajor axis (0.15 au). HATS-8 *b* (Bayliss et al. 2015) and WASP-193 *b* (Barkaoui et al. 2024) are also puffy super-Neptune exoplanets; however, their equilibrium temperatures exceed 1000 K. Remarkably, WASP-193 *b* has the lowest density among all super-Neptunes. This restricted sample of puffy super-Neptunes with precisely measured masses and radii makes TOI-1173 A *b* a valuable addition to this population.

Figure 7 is limited to the giant planets in the range of 0.01–10 $M_{\rm Jup}$ and 0.1–1.33 $R_{\rm Jup}$. From this figure, we observe that TOI-1173 A *b*, along with other super-Neptunes, lies in a transition region. On one side are the low-mass, nondegenerate planets, where the bulk density decreases with increasing mass. On the other side are the high-mass, partially degenerate gas giants, where the bulk density increases with increasing mass. Exoplanets in this region are extremely important, as they allow us to explore the properties of planets that have not undergone runaway gas accretion.

When compared with planets in wide binary systems, TOI-1173 A *b* is the only low-density super-Neptune reported to date. The fundamental parameters of this sample of planet-hosting wide binaries were estimated using high-resolution ($R > 50{,}000$) and high-SNR (> 200) spectroscopy. They represent the best-characterized sample at present, for which precise masses and radii have been obtained through both radial velocity and transit observations. These exoplanets are: WASP-3 A *b* (Bonomo et al. 2017; Behmard et al. 2023), HAT-P-1 B *b* (Liu et al. 2014; Turner et al. 2016), WASP-94 A *b* (Neveu-VanMalle et al. 2014; Teske et al. 2016), HD 80606 *b* (Bonomo et al. 2017; Behmard et al. 2023), WASP-160 B *b* (Lendl et al. 2019; Jofré et al. 2021), WASP-127 A *b* (Seidel et al. 2020; Behmard et al. 2023), HAT-P-4 *b* (Bonomo et al. 2017; Saffe et al. 2017), HD 202772 A *b* (Wang et al. 2019; Behmard et al. 2023), Kepler-25 B *b* and *c* (Mills et al. 2019; Behmard et al. 2023), KELT-2 A *b* (Stassun et al. 2017; Behmard et al. 2023), XO-2N *b* (Teske et al. 2015; Bonomo et al. 2017), WASP-173 *b* (Labadie-Bartz et al. 2019; Behmard et al. 2023), WASP-180 A *b* (Temple et al. 2019; Behmard et al. 2023), and WASP-64 *b* (Bonomo et al. 2017; Behmard et al. 2023). Only two of these exoplanets have a mass below 20 $M_{\oplus}$, but with densities $\rho > 0.3$ g cm^{-3}, depicted as circles in Figure 6. Within the super-Neptune regime, there exists only one wide binary with two exoplanets, Kepler-25 B *b* and *c*. However, these exoplanets have substantially higher densities ($\rho \geqslant 0.5$ g cm^{-3}). This makes TOI-1173 A *b* a potentially unique target for exploring planet formation in wide binary systems.

In the remainder of this section, we investigate different hypotheses to explain the puffy nature of TOI-1173 A *b*.

4.1.1. Stellar Insolation

It is well known that the inflated radii of some hot Jupiters ($M \geqslant 0.3\ M_{\rm Jup}$, $P < 10$ days, and $T_{\rm eq} > 1000$ K) are primarily attributed to the high incident stellar flux upon these planets

Table 3
Orbital and Physical Parameters Derived for TOI-1173 A *b*

	Parameter	Values	Prior
Model-fitted Planetary Parameters			
Orbital period (days)…	P_b	$7.06466^{+0.00028}_{-0.00029}$	$\mathcal{U}(7.0524, 7.0724)$
Time of inferior conjunction (d–2457000)…	$T_{0;b}$	$1702.8444^{+0.0023}_{-0.0023}$	$\mathcal{U}(1688.662, 1688.762)$
Doppler-induced radial velocity semi-amplitude (m s^{-1})…	K_b	$9.67^{+0.47}_{-0.46}$	$\mathcal{U}(0, 20)$
First Laplace parameter…	$\sqrt{e_b}\cos\omega_b$	$0.04^{+0.10}_{-0.12}$	$\mathcal{U}(-1, 1)$
Second Laplace parameter…	$\sqrt{e_b}\sin\omega_b$	$0.01^{+0.13}_{-0.13}$	$\mathcal{U}(-1, 1)$
Planet-to-star radius ratio…	$R_b/R_\star$	$0.0900^{+0.0015}_{-0.0013}$	$\mathcal{U}(0, 1)$
Radii sum divided by semimajor axis…	$(R_\star + R_b)/a_b$	$0.0680^{+0.0011}_{-0.0011}$	$\mathcal{U}(0, 1)$
Cosine of the orbital inclination…	$\cos i_b$	$0.0484^{+0.0016}_{-0.0016}$	$\mathcal{U}(0, 1)$
Transformed limb darkening…	$q_{1;\mathrm{TESS}}$	$0.28^{+0.17}_{-0.11}$	$\mathcal{U}(0, 1)$
Transformed limb darkening…	$q_{2;\mathrm{TESS}}$	$0.36^{+0.38}_{-0.27}$	$\mathcal{U}(0, 1)$
TESS jitter (ppm)…	$\ln\sigma_{\mathrm{TESS}}$	-6.721 ± 0.023	$\mathcal{U}(-15, 0)$
MAROON-X Blue channel jitter (km s^{-1})…	$\ln\sigma_{\mathrm{jit.;\ Blue}}$	$-10.7^{+2.6}_{-2.8}$	$\mathcal{U}(-15, 0)$
MAROON-X Red channel jitter (km s^{-1})…	$\ln\sigma_{\mathrm{jit.;\ Red}}$	$-10.3^{+2.8}_{-3.1}$	$\mathcal{U}(-15, 0)$
HIRES jitter (km s^{-1})…	$\ln\sigma_{\mathrm{jit.;\ HIRES}}$	$-5.88^{+0.24}_{-0.24}$	$\mathcal{U}(-15, 0)$
MAROON-X Blue barycenter motion (km s^{-1} day^{-1})…	$\gamma_{1;\mathrm{Blue}}$	-0.00321 ± 0.00060	$\mathcal{U}(-1000, 1000)$
MAROON-X Red barycenter motion (km s^{-1} day^{-1})…	$\gamma_{1;\mathrm{Red}}$	-0.00448 ± 0.00096	$\mathcal{U}(-1000, 1000)$
HIRES barycenter motion (km s^{-1} day^{-1})…	$\gamma_{1;\mathrm{HIRES}}$	0.0006 ± 0.0018	$\mathcal{U}(-1000, 1000)$
MAROON-X Blue radial velocity slope (km s^{-1} day^{-2})…	$\dot{\gamma}_{1;\mathrm{Blue}}$	-0.0000 ± 0.0011	$\mathcal{U}(-100, 100)$
MAROON-X Red radial velocity slope (km s^{-1} day^{-2})…	$\dot{\gamma}_{1;\mathrm{Red}}$	0.0047 ± 0.0018	$\mathcal{U}(-100, 100)$
HIRES radial velocity slope (km s^{-1} day^{-2})…	$\dot{\gamma}_{1;\mathrm{HIRES}}$	-0.0034 ± 0.0026	$\mathcal{U}(-100, 100)$
Derived Planet b Parameters			
Semimajor axis *b* over host radius…	$a_b/R_\star$	$16.02^{+0.25}_{-0.26}$	…
Semimajor axis…	a_b (au)	0.0696 ± 0.0014	…
Mass…	M_b ($M_\oplus$)	27.4 ± 1.7	…
Radius…	R_b ($R_\oplus$)	9.19 ± 0.18	…
Companion density…	ρ_b (cgs)	$0.195^{+0.018}_{-0.017}$	…
Eccentricity…	e	$0.023^{+0.025}_{-0.016}$	…
Orbital Inclination…	i_b (deg)	$87.228^{+0.087}_{-0.091}$	…
Mass ratio ($M_{\mathrm{pl.}}/M_\star$)…	q	0.0000903 ± 0.0000048	…
Impact parameter …	b	$0.771^{+0.020}_{-0.025}$	…
Total transit duration…	$T_{\mathrm{tot;b}}$ (h)	$2.586^{+0.041}_{-0.039}$	…
Companion surface gravity…	g_b (cgs)	314^{+23}_{-22}	…
Equilibrium temperature *b*…	$T_{\mathrm{eq;b}}$ (K)	868 ± 11	…
Insolation flux …	S_{inc} ($S_\oplus$)	132.0 ± 10	…
Limb-darkening coeff.…	$u_{1;\ \mathrm{TESS}}$	$0.40^{+0.29}_{-0.29}$	…
Limb-darkening coeff.…	$u_{2;\ \mathrm{TESS}}$	$0.13^{+0.36}_{-0.34}$	…

Note. $\mathcal{U}(\alpha, \beta)$ stands for a uniform distribution between α and β.

(e.g., Batygin & Stevenson 2010; Pu & Valencia 2017; Thorngren & Fortney 2018). A fraction of the light from the star penetrates deep into the planetary atmosphere, where it is then absorbed, causing its inflation (see Fortney et al. 2021 for more details). However, as seen in Table 3, TOI-1173 A *b* does not share the planetary properties of hot Jupiters, as its insolation and equilibrium temperature are lower.

To ensure a proper comparison with super-Neptunes precisely characterized by transit and radial velocity observations, we have selected stars with temperatures, metallicities, masses, and radii within ±200 K, ±0.2 dex, ±0.2 $M_\odot$, and ±0.2 $R_\odot$ of those of TOI-1173 A. Figure 8 indicates that the super-Neptunes TOI-1173 A *b* and TOI-1420 *b* experience higher incident flux from their host star than other similar gas giants, which suggests that the inflated state of TOI-1173 A *b* could be attributed to stellar insolation. However, assessing whether this insolation is exceptionally high compared to stars with similar properties as TOI-1173 A is challenging, due to the restricted sample size.

4.1.2. Excess of Internal Heat

Various studies have highlighted the impact of internal heat on a planet's radius, indicating that planets with hotter interiors have larger radii and lower densities than those with cooler interiors of the same composition (e.g., Bodenheimer et al. 2001; Batygin & Stevenson 2010; Lopez & Fortney 2014; Millholland 2019). This inflation stems from the internal heat remaining from the formation of the planet rather than external factors. The age of a planet can influence its internal heat, with younger planets naturally having hotter interiors and consequently larger radii. However, in the case of the ∼8 billion-year-old TOI-1173 A/B system, TOI-1173 A *b* has already cooled (Linder et al. 2019). Hence, an alternative mechanism must be responsible for inflating its radius.

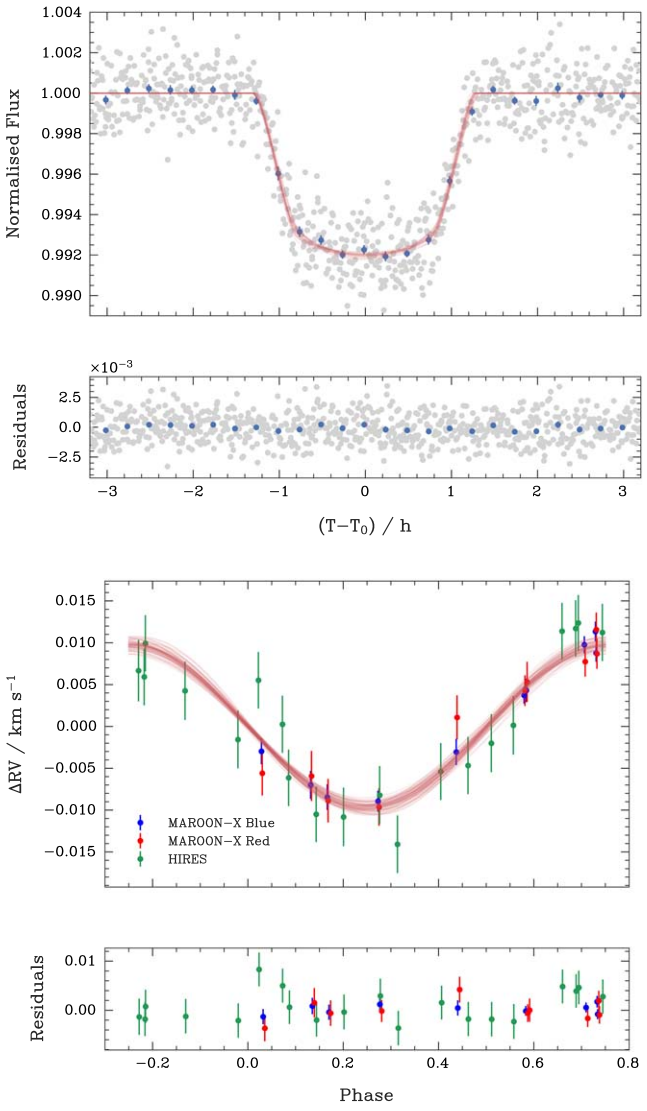

Figure 5. Phase-folded TESS light curve (upper panel) and MAROON-X plus HIRES radial velocities (bottom panel) joint models of TOI-1173A *b*. The red curves show 20 samples drawn from the posterior. The associated residuals are shown below each panel.

4.1.3. Tidal Heating

Tidal heating results from gravitational forces between celestial bodies, causing internal friction and generating heat within the affected body. Millholland et al. (2020) demonstrated that tidal interactions at 0.1 au can yield tidal luminosities up to $L_{\rm tide} \sim 10^{29}$ erg s^{-1} (refer to their Figure 1). Applying the tidal luminosity expression from Equation (1) in Millholland et al. (2020), we estimate $L_{\rm tide} \sim 10^{23}$ erg s^{-1} (assuming zero obliquity and a reduced tidal quality factor $Q' = 10^5$ for Neptune-like planets; Tittemore & Wisdom 1990; Banfield & Murray 1992) for TOI-1173 A *b*. This suggests the potential for significant tidal heating on the planet.

To further investigate this mechanism, we used the structural model with tidal heating of Millholland (2019). This model incorporates tidal heating effects on planetary structures by considering a two-layer planet model consisting of a heavy element core and an H/He envelope with an Markov Chain Monte Carlo fitting approach. The atmospheric envelope evolution is simulated using the Modules for Experiments in Stellar Astrophysics (MESA) code (Paxton et al. 2011, 2013, 2015, 2018, 2019; Jermyn et al. 2023) within the Sub-Saturns[21] code (Millholland et al. 2020). Figure 9 shows the envelope mass fraction estimates for TOI-1173 A *b*. The colored regions indicate the 2D posterior distributions for $\log_{10} Q'$ and $f_{{\rm env},t}$ obtained from the fitting that includes tidal inflation. The horizontal dashed lines indicate the lower limit of the reduced tidal quality factor ($\log_{10} Q' \sim 5.5$). These distributions assume the measured eccentricities and indicate the results for obliquity $\epsilon = 0°$, 30°, and 60°. The mean and 1σ range of $f_{\rm env}$, 0 inferred when neglecting tides are shown with the gray line and bar.

Our findings indicate that when not considering tidal effects, TOI-1173 A *b* has an envelope mass fraction $f_{\rm env}$, 0 of $48.4\% \pm 0.3\%$. However, incorporating tidal heating into the model led to a significant decrease in the estimated envelope mass fraction, ranging from $f_{\rm env}$, $t = 18\%$–40% for $\epsilon = 30°$–60°. This reduction in the envelope mass fraction is attributed to the impact of the tidal inflation resulting from eccentricity and obliquity tides. For $\epsilon = 0°$, it seems that tidal heating has no impact on the planet, as the 2D posterior distribution is below the lower limit of the estimated reduced tidal quality factor $\log_{10} Q' = 5.5$ (horizontal dashed lines in Figure 9).

4.1.4. Planetary Rings

Piro & Vissapragada (2020) suggested that the inflated radii of low-density puffy planets could be a result of planetary rings, which would cause deeper-than-expected transits. This hypothesis is contingent upon the rings being at an oblique angle to the planet's orbital plane. Additionally, if the planet is tidally locked, the impact on the overall transit depth would be negligible. Using Equation (11) from Piro & Vissapragada (2020), we determined a synchronous timescale of 0.061 Myr for TOI-1173 A *b*, confirming its tidal locking. If TOI-1173 A *b* has rings, they would lie in its orbital plane and thus be observed edge-on from our vantage point, thus not explaining the apparent inflated radius. Moreover, because of the planet's proximity to its host star, the rings would be susceptible to dissipating or collapsing under various gravitational forces and interactions (Ohta et al. 2009).

4.1.5. Mass Loss by Atmospheric Escape

Given the relatively high stellar irradiation of TOI-1173 A *b* (see Figure 8) and its proximity to its star, it is reasonable to assume that the planet is losing mass. Therefore, the inflated radius may also be attributed to material evaporating and leaving the planet (e.g., Guo 2013; Ehrenreich et al. 2015; Koskinen et al. 2022). Fossati et al. (2017) demonstrated that it is possible to use theoretical models of mass loss to infer whether atmospheric escape is significant on a planet. Using their Equation (10), we computed the restricted Jeans escape parameter as $\Lambda = 27$. Fossati et al. (2017) show in their Figure 4 that Λ values below the threshold value of $\Lambda_T = 15$–35 correspond to significant atmospheric loss. Consequently, TOI-1173 A *b* might be losing its atmosphere. However, it is important to highlight that this possibility is only speculative at the moment, given the lack of transmission spectroscopy or multiband transit photometry for TOI-1173 A *b*. Mass-loss measurements are necessary for confirmation, as previously mentioned in Section 1.

[21] https://github.com/smillholland/Sub-Saturns/

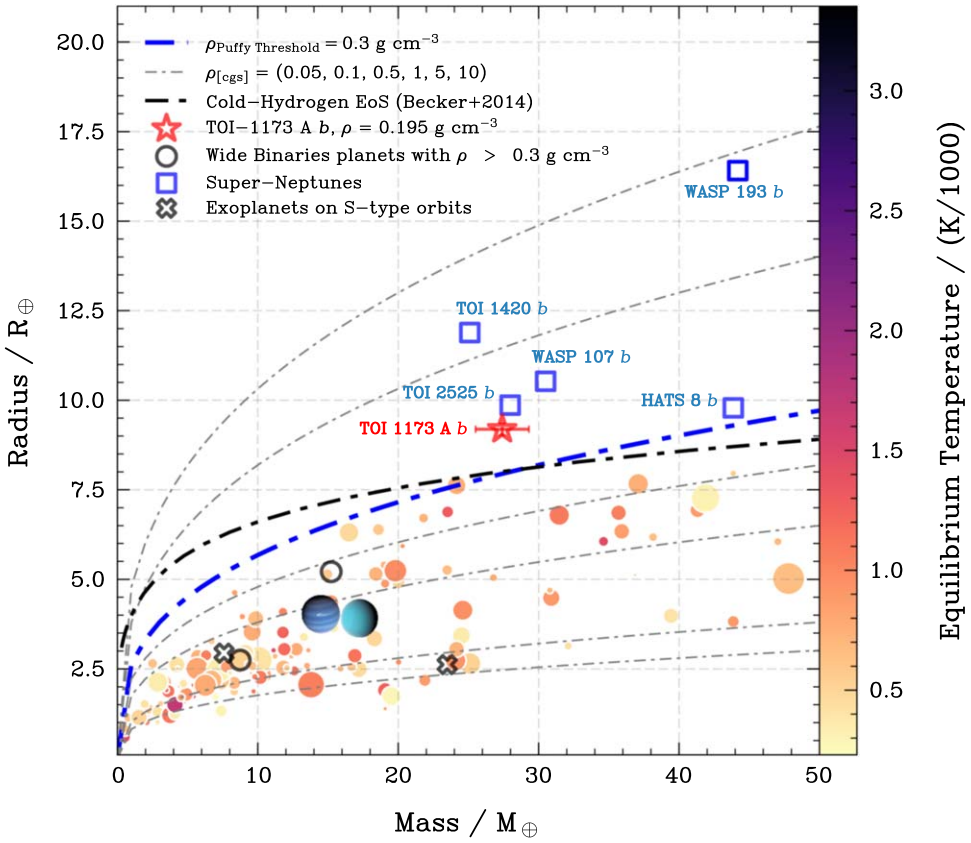

Figure 6. M–R distribution (colored by the planet's equilibrium temperature and sized by the orbital eccentricity) for confirmed exoplanets presented in the Encyclopædia of Exoplanetary Systems (https://exoplanet.eu/home/) as of 2024 March. The red star represents TOI-1173 A *b*, and the dashed black line is the theoretical M–R curve for a planet composed of cold Hydrogen according to the H-REOS.3 equation of state from Becker et al. (2014), to which TOI-1173 A *b*'s composition seems to be alike. Constant-density curves are shown with the dotted–dashed lines, and the blue one represents the density threshold adopted in this work for puffy planets. In terms of period, semimajor axis, and mass, TOI-1173 A *b* is similar to TOI-1420 *b* and WASP-107 *b*. The black open circles represent the planets from the wide binary sample with densities higher than 0.3 g cm^{-3}, while the black crosses represent planets on S-type orbits (planets that orbit just one star in a binary pair) with masses between 5 and 35 $M_\oplus$.

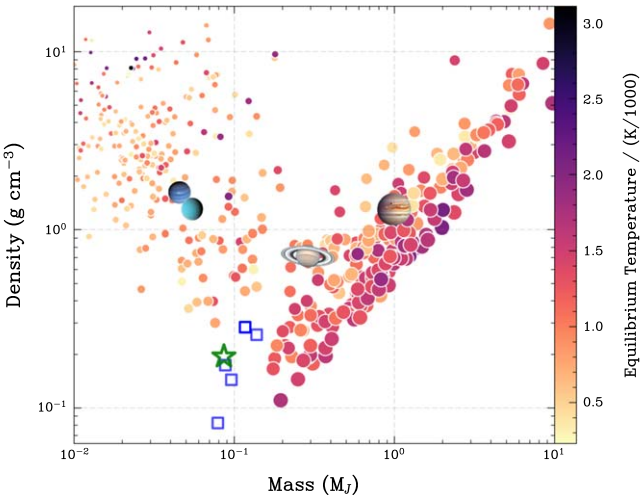

Figure 7. Planetary density as a function of the planetary mass of exoplanets obtained from the Encyclopædia of Exoplanetary Systems as of 2024 March. The characteristic "V" shape, and the size of the points, which scale with the planetary radius, denote two regimes of planets. The circles are colored according to their equilibrium temperature. TOI-1173 A *b* (green star) and the other puffy super-Neptunes (open blue squares) lie in the transition region.

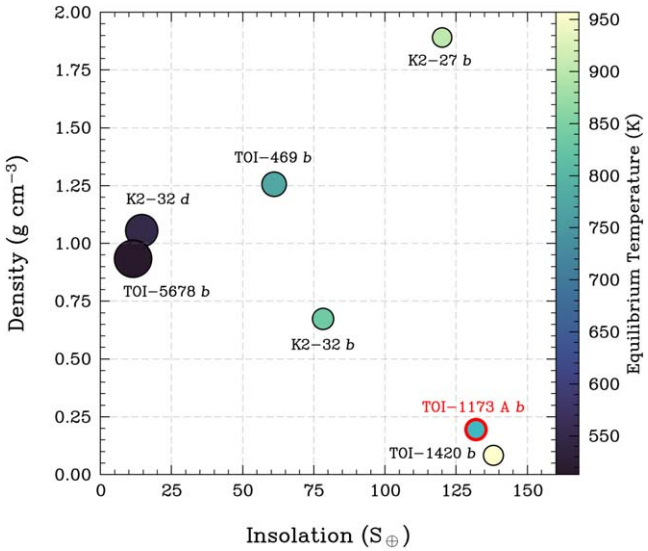

Figure 8. Planet density as a function of stellar insolation. TOI-1173 A *b* is indicated in red. The circles represent the planets with host stars sharing similar physical parameters as TOI-1173 A, colored by their equilibrium temperatures and sized by the planet's semimajor axis.

4.1.6. Other Causes of the Anomalously Large Radius

Alternatively, explanations like high-altitude dust or hazes have been suggested to account for the inflated radii of super-Neptunes (e.g., Wang & Dai 2019; Gao & Zhang 2020). However, with our current data, it is challenging to confirm if any of these mechanisms could be responsible for inflating the

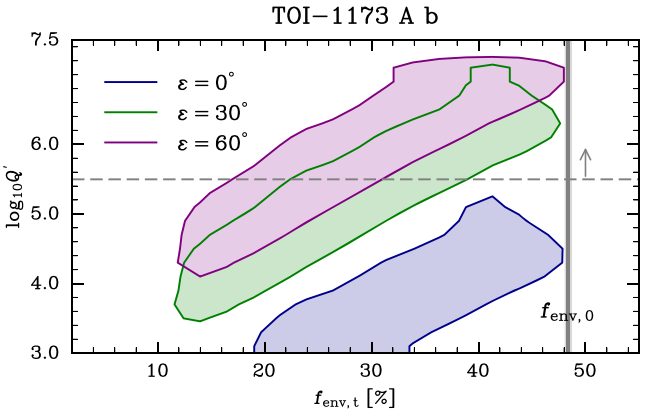

Figure 9. Envelope mass fraction estimates with tides ($f_{\rm env}$, t) and without tides ($f_{\rm env}$, 0) of TOI-1173 A b. The horizontal dashed lines represent the lower limit of the reduced tidal quality factor ($\log_{10} Q'$). The mean and standard deviation of $f_{\rm env}$, 0 are represented by the vertical gray bar. The colored regions indicate the 2σ contours of the posterior distributions of $\log_{10} Q'$ and $f_{\rm env,\,t}$ after accounting for tides.

radius of TOI-1173 A b, so transmission spectroscopy is deemed necessary and encouraged for a more conclusive understanding of the planet's atmospheric physics.

4.2. Dynamical Timescales

In the following, we explore noteworthy features of the interactions between TOI-1173 A and its companion, focusing on turbulent friction, magnetic field maintenance, and orbital dynamics. When a perturbation occurs, interactions with the primary star can serve as a damping mechanism, effectively obliterating past effects, particularly if these interactions are on a comparable timescale to the age of the system. This phenomenon can be investigated through consideration of the dynamical timescales derived from the mass of the system components (primary star, secondary star, and the planet), the degree of tidal detachment, and their respective orbital eccentricities.

4.2.1. Orbital Eccentricity Evolution

We considered the timescale on which TOI-1173 A b's orbital eccentricity might have evolved over time, expressed by the ratio $\tau_e \sim e/(de/dt)$, following the framework presented by Rice et al. (2022)—see Equations (6)–(13). We measured an eccentricity of 0.023 for TOI-1173 A b, and it is worth noting that, over time, planets are anticipated to circularize their orbits, especially due to energy loss caused by tidal dissipation (Dawson & Johnson 2018). We adopted in this case a tidal dissipation parameter within the range $Q' = 10^4$–10^6 and $\kappa_2 = 0.3$ as the Love number, in line with Penev et al. (2018) and Rice et al. (2022). Note that a value of Q' in this range is also supported by the results obtained in Section 4.1.2 using the tidal heating model of Millholland et al. (2020).

Based on the physical and orbital parameters of TOI-1173 A b—namely, the orbital period P_b, eccentricity e, semimajor axis a_b, and mass M_b (see Table 3)—we calculated a tidal circularization timescale of $\tau_e \approx 10^8$–10^{10} yr for TOI-1173 A b.

Relative to the system's age, the tidal circularization timescale could be as short as 100 Myr, which is much less than the age of the planet ($\Gamma \sim 8.7$ Gyr). Therefore, it is plausible that TOI-1173 A b may have exhibited a higher eccentricity in the past, and it was subsequently dampened after a few billion years. On the other hand, the circularization timescale may also be much longer, such that in this case, no evolution in eccentricity over the planet's lifetime would be expected. Since the derived eccentricity of TOI-1173 A b today is consistent with zero at the 1.5 σ level, we cannot draw strong conclusions about the original eccentricity of its orbit at formation.

4.2.2. Perturbations due to a Tertiary Companion

The planet's orbit may even have the potential to adopt a low-eccentricity arrangement through von-Zeipel–Lidov–Kozai (vZLK) cycles due to interactions with a tertiary companion (see Rice et al. 2023). Adopting a quadrupole level of approximation, and considering that the planet's mass is considerably smaller than the proper masses of the binary stars, we used Equation (27) in Naoz (2016) to estimate the timescale at which the vZLK process may play a part in the evolution of TOI-1173 A b.

Because the eccentricity for the TOI-1173 A/B system is uncertain, to estimate $\tau_{\rm vZLK}$, we considered e_B ranging from 0.0 to 0.9. At the current architecture, we estimated the timescale for vZLK perturbations in the order of $\tau_{\rm vZLK,e=0} \sim 10^{13}$ yr, and $\tau_{\rm vZLK,e=0.9} \sim 10^{12}$ yr. Comparing those parameters with the system's age, we observed that the timescale is bigger than Γ, much longer than the age of the Universe in the null-eccentricity case, indicating that vZLK migration might not have significantly influenced the system's evolution if TOI-1173 A b originated near its present location, i.e., its damping timescale is sufficiently large to be unobserved.

Interestingly, when extrapolating its initial position for $P_b = 1$ yr, a Jupiter-like current location with $P_b \sim 12$ yr, or Saturn-like with $P_b \sim 30$ yr, $\tau_{\rm vZLK}$ ranges between $\sim 10^{11}$ and $\sim 10^8$ yr. If the planet initially formed far away from its current position, consistent with theories of giant planet formation (D'Angelo & Lubow 2008; Batygin & Laughlin 2015, and references therein), $\tau_{\rm vZLK}$ approaches Γ, indicating the possibility of past migration through vZLK mechanisms.

4.2.3. Apsidal Precession due to General Relativity

vZLK oscillations can however be dampened by additional perturbations that induce apsidal precession at a faster rate, thereby diminishing the orbit-averaged torque exerted by the companion star (Wu & Murray 2003). As for apsidal precession arising from general relativity, the dampening timescale is given in Equation (29) in Rice et al. (2023).

For TOI-1173 A b, we estimated $\tau_{\rm GR} \sim 10^4$ yr—a short timescale when compared to both $\tau_{\rm vZLK}$ and the system's age. This effectively eliminates the possibility of the system undergoing vZLK oscillations, as the influence of general relativity on apsidal precession is substantially faster when compared to the system's age.

5. Conclusions and Future Work

We present the discovery of TOI-1173 A b, the first super-Neptune ($M = 27.4 M_\oplus$) with a highly inflated radius ($R = 9.19 R_\oplus$) in a wide binary system (projected separation ~11,400 au). TESS photometry and radial velocity observations with the MAROON-X and HIRES spectrographs revealed a planet on a nearly circular ($e = 0.023$) close-in orbit ($P = 7.064$ days, $a = 0.069$ au) to the primary star. Additionally, we infer a density of $\rho = 0.195$ g cm^{-3}, equilibrium temperature

$T_{\rm eq} = 868$ K, and insolation flux $S_{\oplus} = 132$ for the planet. TOI-1173 A *b* stands out as the only low-density super-Neptune in a binary system reported to date.

Hypotheses exploring the causes of the planet's inflated nature include stellar insolation, excess internal heat, the presence of planetary rings, and the potential mass loss by atmospheric escape. Although stellar insolation, internal heat, and mass loss may contribute (see Section 4.1), we highlighted the negligible impact of planetary rings due to the planet's tidally locked nature. Therefore, we conclude that the most promising scenario to explain the inflated radius of TOI-1173 A *b* is tidal heating.

We investigated the dynamical evolution of TOI-1173 A and its planetary companion, examining factors such as the eccentricity evolution influenced by tidal dissipation, the impact of tertiary companions, and the role of general-relativity-induced apsidal precession (see Section 4.2).

Whether the system was born aligned or misaligned, however, is uncertain with current data, and TOI-1173 A *b* represents a benchmark follow-up case for further analysis via the Rossiter–McLaughlin (RM) effect. Following the framework in Triaud (2018), we estimated an expected RM amplitude of $\sim 6\,{\rm m\,s^{-1}}$ for TOI-1173 A *b*, so that the system could be observed with current extreme-precision spectrographs such as the Keck Planet Finder (Gibson et al. 2016), the EXtreme PREcision Spectrometer (Blackman et al. 2020), and/or MAROON-X (Seifahrt et al. 2018).

The relative comparability between the tidal circularization timescale and the system's age, expressed as $\tau_e \sim \Gamma$, leaves us without a clear conclusion as to whether the system exhibited a high eccentricity in the past. Under these highly eccentric configurations, other possible formation mechanisms include single planet–planet scattering events (e.g., Rasio & Ford 1996; Chatterjee et al. 2008) and resonant interactions (Naoz et al. 2011; Petrovich & Tremaine 2016), while low eccentricities are usually associated with high multiplicity, as in our own solar system (e.g., Lissauer 1993; Ford & Rasio 2008; Limbach & Turner 2015; Van Eylen & Albrecht 2015), or smooth disk migration (Goldreich & Sari 2003; Lega et al. 2021). With $\tau_{\rm vZLK} > \Gamma$, TOI-1173 A *b* might have undergone migration through this mechanism; however, the possibility of current vZLK oscillations occurring in the system is eliminated, given that the apsidal precession timescale due to general relativity is orders of magnitude smaller than the proper vZLK timescale ($\tau_{\rm GR} \ll \tau_{\rm vZLK}$).

Looking ahead, the low mass and density of TOI-1173 A *b*, along with TOI-2525 *b*, WASP-107 *b*, TOI-1420 *b*, HATS-8 *b*, and WASP-193 *b*, make it a key planet for atmospheric and dynamical characterization, with further analysis necessary and encouraged to uncover its extreme atmospheric physics in detail, as well as to reveal its past orbital configuration.

Acknowledgments

J.Y.G. acknowledges support from a Carnegie Fellowship. T.F. acknowledges support from the Yale Graduate School of Arts and Sciences. D.L.O. acknowledges support from CNPq (PCI 301612/2024-2). H.R. acknowledges the support from NOIRLab, which is managed by the Association of Universities for Research in Astronomy (AURA) under a cooperative agreement with the National Science Foundation.

This work has made use of data collected with the Gemini Telescope. This research has made use of the Keck Observatory Archive (KOA), which is operated by the W. M. Keck Observatory and the NASA Exoplanet Science Institute (NExScI), under contract with the National Aeronautics and Space Administration. This paper includes data collected by the TESS mission. Funding for the TESS mission is provided by NASA's Science Mission Directorate. This research has made use of the Exoplanet Follow-up Observation Program (ExoFOP; doi:10.26134/ExoFOP5) website, which is operated by the California Institute of Technology, under contract with the National Aeronautics and Space Administration under the Exoplanet Exploration Program. Some of the data presented herein were obtained at the Keck Observatory, which is a private 501(c)3 non-profit organization operated as a scientific partnership among the California Institute of Technology, the University of California, and the National Aeronautics and Space Administration. The Observatory was made possible by the generous financial support of the W. M. Keck Foundation. The authors wish to recognize and acknowledge the very significant cultural role and reverence that the summit of Maunakea has always had within the Native Hawaiian community. We are most fortunate to have the opportunity to conduct observations from this mountain. Some of the data presented in this paper were obtained from the Mikulski Archive for Space Telescopes (MAST) at the Space Telescope Science Institute. The specific observations analyzed can be accessed via doi:10.17909/dpx3-gv19. STScI is operated by the Association of Universities for Research in Astronomy, Inc., under NASA contract NAS526555. Support to MAST for these data is provided by the NASA Office of Space Science via grant NAG57584 and by other grants and contracts.

Facilities: Gemini:Gillett (MAROON-X), Keck:I (HIRES), TESS.

Software: NUMPY (van der Walt et al. 2011), MATPLOTLIB (Hunter 2007), PANDAS (McKinney 2010), LIGHTKURVE (Lightkurve Collaboration et al. 2018), SCIPY (Virtanen et al. 2020), JULIET (Espinoza et al. 2019), ASTROML (Ivezić et al. 2014), DYNESTY (Speagle 2020), ALLESFITTER (Günther & Daylan 2021), ASTROBASE (Bhatti & Bouma 2021), SERVAL (Zechmeister et al. 2020), MESA (Paxton et al. 2019), EMCEE (Foreman-Mackey et al. 2013), SUB-SATURNS (Millholland et al. 2020), SMPLOTLIB (Li 2023).

ORCID iDs

Jhon Yana Galarza https://orcid.org/0000-0001-9261-8366
Thiago Ferreira https://orcid.org/0000-0003-2059-470X
Diego Lorenzo-Oliveira https://orcid.org/0000-0002-1387-2954
Joshua D. Simon https://orcid.org/0000-0002-4733-4994
Henrique Reggiani https://orcid.org/0000-0001-6533-6179
Anthony L. Piro https://orcid.org/0000-0001-6806-0673
R. Paul Butler https://orcid.org/0000-0003-1305-3761
Yuri Netto https://orcid.org/0000-0003-2636-9378
Adriana Valio https://orcid.org/0000-0002-1671-8370
David R. Ciardi https://orcid.org/0000-0002-5741-3047
Boris Safonov https://orcid.org/0000-0003-1713-3208

References

Aller, A., Lillo-Box, J., Jones, D., Miranda, L. F., & Barceló Forteza, S. 2020, A&A, 635, A128
Anderson, D. R., Collier Cameron, A., Delrez, L., et al. 2017, A&A, 604, A110
Banfield, D., & Murray, N. 1992, Icar, 99, 390
Barkaoui, K., Pozuelos, F. J., Hellier, C., et al. 2024, Nat Astron

Batygin, K., & Laughlin, G. 2015, PNAS, 112, 4214
Batygin, K., & Stevenson, D. J. 2010, ApJL, 714, L238
Bayliss, D., Hartman, J. D., Bakos, G. Á., et al. 2015, AJ, 150, 49
Becker, A., Lorenzen, W., Fortney, J. J., et al. 2014, ApJS, 215, 21
Behmard, A., Dai, F., Brewer, J. M., Berger, T. A., & Howard, A. W. 2023, MNRAS, 521, 2969
Bennett, K. A., Redfield, S., Oklopčić, A., et al. 2023, AJ, 165, 264
Bhatti, W., & Bouma, L. 2021, waqasbhatti/astrobase: astrobase v0.5.3, Zenodo, doi:10.5281/zenodo.4445344
Bitsch, B., Lambrechts, M., & Johansen, A. 2015, A&A, 582, A112
Blackman, R. T., Fischer, D. A., Jurgenson, C. A., et al. 2020, AJ, 159, 238
Bodenheimer, P., Lin, D. N. C., & Mardling, R. A. 2001, ApJ, 548, 466
Bonomo, A. S., Desidera, S., Benatti, S., et al. 2017, A&A, 602, A107
Butler, R. P., Marcy, G. W., Williams, E., et al. 1996, PASP, 108, 500
Butler, R. P., Vogt, S. S., Laughlin, G., et al. 2017, AJ, 153, 208
Cauley, P. W., Redfield, S., & Jensen, A. G. 2017, AJ, 153, 217
Chatterjee, S., Ford, E. B., Matsumura, S., & Rasio, F. A. 2008, ApJ, 686, 580
Christie, D., Arras, P., & Li, Z.-Y. 2013, ApJ, 772, 144
Ciardi, D. R., Beichman, C. A., Horch, E. P., & Howell, S. B. 2015, ApJ, 805, 16
D'Angelo, G., & Lubow, S. H. 2008, ApJ, 685, 560
Dawson, R. I., & Johnson, J. A. 2018, ARA&A, 56, 175
Doazan, V., & Peton, A. 1970, A&A, 9, 245
dos Santos, L. A., Ehrenreich, D., Bourrier, V., et al. 2020, A&A, 640, A29
Ehrenreich, D., Bourrier, V., Wheatley, P. J., et al. 2015, Natur, 522, 459
El-Badry, K., Rix, H.-W., & Heintz, T. M. 2021, MNRAS, 506, 2269
Espinoza, N., & Jordán, A. 2016, MNRAS, 457, 3573
Espinoza, N., Kossakowski, D., & Brahm, R. 2019, MNRAS, 490, 2262
Ford, E. B., & Rasio, F. A. 2008, ApJ, 686, 621
Foreman-Mackey, D., Hogg, D. W., Lang, D., & Goodman, J. 2013, PASP, 125, 306
Fortney, J. J., Dawson, R. I., & Komacek, T. D. 2021, JGRE, 126, e06629
Fossati, L., Erkaev, N. V., Lammer, H., et al. 2017, A&A, 598, A90
Gao, P., & Zhang, X. 2020, ApJ, 890, 93
Gibson, S. R., Howard, A. W., Marcy, G. W., et al. 2016, Proc. SPIE, 9908, 990870
Goldreich, P., & Sari, R. 2003, ApJ, 585, 1024
Guerrero, N. M., Seager, S., Huang, C. X., et al. 2021, ApJS, 254, 39
Günther, M. N., & Daylan, T. 2021, ApJS, 254, 13
Guo, J. H. 2013, ApJ, 766, 102
Hippke, M., David, T. J., Mulders, G. D., & Heller, R. 2019, AJ, 158, 143
Hunter, J. D. 2007, CSE, 9, 90
Ida, S., & Lin, D. N. C. 2004, ApJ, 604, 388
Ivezić, Ž., Connolly, A. J., VanderPlas, J. T., & Gray, A. 2014, Statistics, Data Mining, and Machine Learning in Astronomy: A Practical Python Guide for the Analysis of Survey Data (Princeton, NJ: Princeton Univ. Press)
Jenkins, J. M., Twicken, J. D., McCauliff, S., et al. 2016, Proc. SPIE, 9913, 99133E
Jensen, A. G., Redfield, S., Endl, M., et al. 2012, ApJ, 751, 86
Jermyn, A. S., Bauer, E. B., Schwab, J., et al. 2023, ApJS, 265, 15
Jofré, E., Petrucci, R., Maqueo Chew, Y. G., et al. 2021, AJ, 162, 291
Kipping, D. M. 2013, MNRAS, 435, 2152
Kipping, D. M., Hartman, J., Buchhave, L. A., et al. 2013, ApJ, 770, 101
Kislyakova, K. G., Holmström, M., Odert, P., et al. 2019, A&A, 623, A131
Koskinen, T. T., Lavvas, P., Huang, C., et al. 2022, ApJ, 929, 52
Kovács, G., Zucker, S., & Mazeh, T. 2002, A&A, 391, 369
Krolikowski, D. M., Kraus, A. L., Tofflemire, B. M., et al. 2024, AJ, 167, 79
Labadie-Bartz, J., Rodriguez, J. E., Stassun, K. G., et al. 2019, ApJS, 240, 13
Lee, E. J., & Chiang, E. 2015, ApJ, 811, 41
Lega, E., Nelson, R. P., Morbidelli, A., et al. 2021, A&A, 646, A166
Lendl, M., Anderson, D. R., Bonfanti, A., et al. 2019, MNRAS, 482, 301
Li, J. 2023, AstroJacobLi/smplotlib: v0.0.9, Zenodo, doi:10.5281/zenodo.8126529
Lightkurve Collaboration, Cardoso, J. V. d., Hedges, C., et al. 2018, Lightkurve: Kepler and TESS time series analysis in Python, Astrophysics Source Code Library, ascl:1812.013
Limbach, M. A., & Turner, E. L. 2015, PNAS, 112, 20
Linder, E. F., Mordasini, C., Mollière, P., et al. 2019, A&A, 623, A85
Lissauer, J. J. 1993, ARA&A, 31, 129
Lissauer, J. J., & Stewart, G. R. 1993, in Protostars and Planets III, ed. E. H. Levy & J. I. Lunine (Tucson, AZ: Univ. Arizona Press), 1061
Liu, F., Asplund, M., Ramirez, I., Yong, D., & Melendez, J. 2014, MNRAS, 442, L51
Lopez, E. D., & Fortney, J. J. 2014, ApJ, 792, 1
Lucy, L. B., & Sweeney, M. A. 1971, AJ, 76, 544
Mayor, M., & Queloz, D. 1995, Natur, 378, 355
McKinney, W. 2010, Proc. of the 9th Python in Science Conf., ed. S. van der Walt & J. Millman, (Austin, TX: SciPy), 56
Millholland, S. 2019, ApJ, 886, 72
Millholland, S., Petigura, E., & Batygin, K. 2020, ApJ, 897, 7
Mills, S. M., Howard, A. W., Weiss, L. M., et al. 2019, AJ, 157, 145
Mugrauer, M., Ginski, C., & Seeliger, M. 2014, MNRAS, 439, 1063
Murray-Clay, R. A., Chiang, E. I., & Murray, N. 2009, ApJ, 693, 23
Naoz, S. 2016, ARA&A, 54, 441
Naoz, S., Farr, W. M., Lithwick, Y., Rasio, F. A., & Teyssandier, J. 2011, Natur, 473, 187
Neveu-VanMalle, M., Queloz, D., Anderson, D. R., et al. 2014, A&A, 572, A49
Ohno, K., & Tanaka, Y. A. 2021, ApJ, 920, 124
Ohta, Y., Taruya, A., & Suto, Y. 2009, ApJ, 690, 1
Orell-Miquel, J., Murgas, F., Pallé, E., et al. 2022, A&A, 659, A55
Owen, J. E., Murray-Clay, R. A., Schreyer, E., et al. 2023, MNRAS, 518, 4357
Owen, J. E., & Wu, Y. 2013, ApJ, 775, 105
Paxton, B., Bildsten, L., Dotter, A., et al. 2011, ApJS, 192, 3
Paxton, B., Cantiello, M., Arras, P., et al. 2013, ApJS, 208, 4
Paxton, B., Marchant, P., Schwab, J., et al. 2015, ApJS, 220, 15
Paxton, B., Schwab, J., Bauer, E. B., et al. 2018, ApJS, 234, 34
Paxton, B., Smolec, R., Schwab, J., et al. 2019, ApJS, 243, 10
Penev, K., Bouma, L. G., Winn, J. N., & Hartman, J. D. 2018, AJ, 155, 165
Petrovich, C., & Tremaine, S. 2016, ApJ, 829, 132
Piaulet, C., Benneke, B., Rubenzahl, R. A., et al. 2021, AJ, 161, 70
Piro, A. L., & Vissapragada, S. 2020, AJ, 159, 131
Pollack, J. B., Hubickyj, O., Bodenheimer, P., et al. 1996, Icar, 124, 62
Pu, B., & Valencia, D. 2017, ApJ, 846, 47
Rasio, F. A., & Ford, E. B. 1996, Sci, 274, 954
Rice, M., Wang, S., Gerbig, K., et al. 2023, AJ, 165, 65
Rice, M., Wang, S., & Laughlin, G. 2022, ApJL, 926, L17
Rice, W. K. M., & Armitage, P. J. 2003, ApJL, 598, L55
Ricker, G. R., Winn, J. N., Vanderspek, R., et al. 2015, JATIS, 1, 014003
Saffe, C., Jofré, E., Martioli, E., et al. 2017, A&A, 604, L4
Safonov, B. S., Lysenko, P. A., & Dodin, A. V. 2017, AstL, 43, 344
Seidel, J. V., Lendl, M., Bourrier, V., et al. 2020, A&A, 643, A45
Seifahrt, A., Bean, J. L., Kasper, D., et al. 2022, Proc. SPIE, 12184, 121841G
Seifahrt, A., Stürmer, J., Bean, J. L., & Schwab, C. 2018, Proc. SPIE, 10702, 107026D
Smith, J. C., Stumpe, M. C., Van Cleve, J. E., et al. 2012, PASP, 124, 1000
Sobolev, V. V. 1960, Moving Envelopes of Stars, Vol. 10 (Cambridge, MA: Harvard Univ. Press)
Spake, J. J., Sing, D. K., Evans, T. M., et al. 2018, Natur, 557, 68
Speagle, J. S. 2020, MNRAS, 493, 3132
Stassun, K. G., Collins, K. A., & Gaudi, B. S. 2017, AJ, 153, 136
Stumpe, M. C., Smith, J. C., Van Cleve, J. E., et al. 2012, PASP, 124, 985
Temple, L. Y., Hellier, C., Anderson, D. R., et al. 2019, MNRAS, 490, 2467
Teske, J. K., Ghezzi, L., Cunha, K., et al. 2015, ApJL, 801, L10
Teske, J. K., Khanal, S., & Ramírez, I. 2016, ApJ, 819, 19
Thorngren, D. P., & Fortney, J. J. 2018, AJ, 155, 214
Tittemore, W. C., & Wisdom, J. 1990, Icar, 85, 394
Triaud, A. H. M. J. 2018, in Handbook of Exoplanets, ed. H. J. Deeg & J. A. Belmonte (Berlin: Springer), 1375
Trifonov, T., Brahm, R., Jordán, A., et al. 2023, AJ, 165, 179
Turner, J. D., Pearson, K. A., Biddle, L. I., et al. 2016, MNRAS, 459, 789
van der Walt, S., Colbert, S. C., & Varoquaux, G. 2011, CSE, 13, 22
Van Eylen, V., & Albrecht, S. 2015, ApJ, 808, 126
Virtanen, P., Gommers, R., Oliphant, T. E., et al. 2020, NatMe, 17, 261
Vissapragada, S., Knutson, H. A., Jovanovic, N., et al. 2020, AJ, 159, 278
Vogt, S. S., Allen, S. L., Bigelow, B. C., et al. 1994, Proc. SPIE, 2198, 362
Wang, L., & Dai, F. 2019, ApJL, 873, L1
Wang, S., Jones, M., Shporer, A., et al. 2019, AJ, 157, 51
Wizinowich, P., Acton, D. S., Shelton, C., et al. 2000, PASP, 112, 315
Wu, Y., & Murray, N. 2003, ApJ, 589, 605
Yoshida, S., Vissapragada, S., Latham, D. W., et al. 2023, AJ, 166, 181
Zechmeister, M., & Kürster, M. 2009, A&A, 496, 577
Zechmeister, M., Reiners, A., Amado, P. J., et al. 2018, A&A, 609, A12
Zechmeister, M., Reiners, A., Amado, P. J., et al. 2020, SERVAL: SpEctrum Radial Velocity AnaLyser, Astrophysics Source Code Library, ascl:2006.011